

# Mapping the Excited State Potential Energy Surface of a Retinal Chromophore Model with Multireference and Equation-of-Motion Coupled-Cluster Methods

Samer Gozem,<sup>†</sup> Federico Melaccio,<sup>‡</sup> Roland Lindh,<sup>§</sup> Anna I. Krylov,<sup>⊥</sup> Alexander A. Granovsky,<sup>○</sup> Celestino Angeli,<sup>||</sup> and Massimo Olivucci<sup>\*,†,‡</sup>

<sup>†</sup>Department of Chemistry, Bowling Green State University, Bowling Green, Ohio 43403, United States

<sup>‡</sup>Dipartimento di Biotecnologie, Chimica e Farmacia, Università di Siena, via A. Moro 2, I-53100 Siena, Italy

<sup>§</sup>Department of Chemistry, Ångström, the Theoretical Chemistry Programme, POB 518, SE-751 20 Uppsala, Sweden

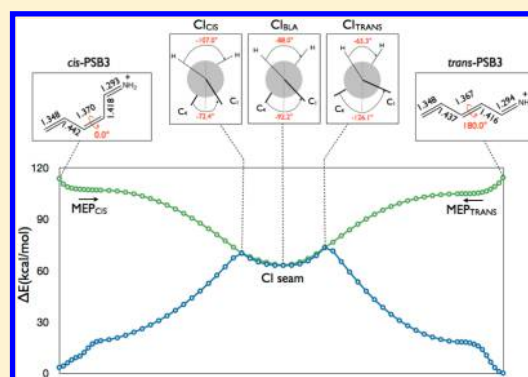
<sup>⊥</sup>Department of Chemistry, University of Southern California, Los Angeles, California 90089-0482, United States

<sup>○</sup>Firefly Project, Moscow 117593, Russia

<sup>||</sup>Dipartimento di Chimica, Università di Ferrara, via Borsari 46, I-44121 Ferrara, Italy

## S Supporting Information

**ABSTRACT:** The photoisomerization of the retinal chromophore of visual pigments proceeds along a complex reaction coordinate on a multidimensional surface that comprises a hydrogen-out-of-plane (HOOP) coordinate, a bond length alternation (BLA) coordinate, a single bond torsion and, finally, the reactive double bond torsion. These degrees of freedom are coupled with changes in the electronic structure of the chromophore and, therefore, the computational investigation of the photochemistry of such systems requires the use of a methodology capable of describing electronic structure changes along all those coordinates. Here, we employ the penta-2,4-dieniminium (PSB3) cation as a minimal model of the retinal chromophore of visual pigments and compare its excited state isomerization paths at the CASSCF and CASPT2 levels of theory. These paths connect the *cis* isomer and the *trans* isomer of PSB3 with two structurally and energetically distinct conical intersections (CIs) that belong to the same intersection space. MRCISD+Q energy profiles along these paths provide benchmark values against which other ab initio methods are validated. Accordingly, we compare the energy profiles of MRPT2 methods (CASPT2, QD-NEVPT2, and XMCQDPT2) and EOM-SF-CC methods (EOM-SF-CCSD and EOM-SF-CCSD(dT)) to the MRCISD+Q reference profiles. We find that the paths produced with CASSCF and CASPT2 are topologically and energetically different, partially due to the existence of a “locally excited” region on the CASPT2 excited state near the Franck–Condon point that is absent in CASSCF and that involves a single bond, rather than double bond, torsion. We also find that MRPT2 methods as well as EOM-SF-CCSD(dT) are capable of quantitatively describing the processes involved in the photoisomerization of systems like PSB3.



## INTRODUCTION

The penta-2,4-dieniminium cation (PSB3, see Scheme 1) is a conjugated and protonated imine which has been used extensively as a computational model of the retinal protonated Schiff base chromophore (rPSB) of visual pigments.<sup>1–4</sup> Recently, we benchmarked the effect of dynamic electron correlation along three paths spanning the ground state (*S*<sub>0</sub>) potential energy surface (PES) of PSB3 using several electronic structure methods. These included multireference configuration interaction with single and double excitations<sup>5,6</sup> (MRCISD) with and without the Davidson correction *Q*,<sup>7</sup> multireference second order perturbation theory (MRPT2) methods in ref 8, equation-of-motion coupled-cluster (EOM-CC) methods<sup>9,10</sup> in ref 11, and an *a posteriori* spin-decontamination procedure on

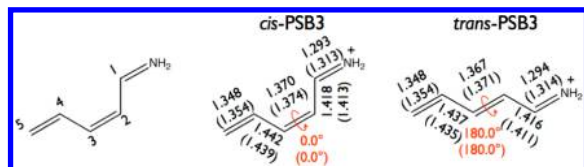
top of a spin-flip time-dependent density functional theory (TD-DFT) approach in ref 12.

In the present contribution, we map a different region of the PES, this time focusing on three paths generated on the first singlet excited state (*S*<sub>1</sub>) state rather than the *S*<sub>0</sub> state. Two paths (named MEP<sub>CIS</sub> and MEP<sub>TRANS</sub>) lead from the Franck–Condon (FC) point of one isomer of PSB3 (*cis*- or *trans*-PSB3, shown in Scheme 1) to a conical intersection (CI). MEP<sub>CIS</sub> is similar to the path already computed in ref 13. The third path is along a seam of CIs that connects the two above paths; this path is named the CI seam path. Note that while the first two paths are actual reaction paths on the PES, the third is

Received: June 2, 2013

Published: August 14, 2013

Scheme 1. (left) Structure of PSB3 Showing Numbering of Atoms. (center and right) Geometric Parameters for the *cis* and *trans* Isomers of PSB3 Computed with CASSCF and CASPT2<sup>a</sup>



<sup>a</sup>CASPT2 geometry parameters are shown in parentheses. Bond length values are in angstroms and are displayed in black while torsions are displayed in red.

artificially constructed by an interpolation of coordinates (see the Methods section).

Upon photoexcitation, PSB3 undergoes a partial transfer of its positive charge from the  $=\text{C}_2\text{H}-\text{C}_1\text{H}=\text{NH}_2$  side (the Schiff base moiety) to the  $\text{C}_5\text{H}_2=\text{C}_4\text{H}-\text{C}_3\text{H}=\text{}$  side of the molecule (the allyl moiety).<sup>1</sup> Studies of PSB3 conducted at the CASSCF level of theory show a barrierless path leading from the FC point to a CI.<sup>2</sup> In fact, Migani et al. mapped a path on the  $S_1$  PES of PSB3 at the CASSCF level of theory by following a minimum energy path (MEP) coordinate along the  $S_1$  surface starting from the FC point of *cis*-PSB3.<sup>13</sup> However, after an early report by Page et al.,<sup>14</sup> a number of studies have emerged showing inconsistencies between CASSCF, which is missing dynamic electron correlation, and higher-level electronic structure methods. Fantacci et al.<sup>15</sup> used the CASSCF paths from Migani et al.<sup>13</sup> to test the effect of running single point CASPT2 and TD-DFT energy calculations along these paths. They found that the barrierless CASSCF path is no longer barrierless when dynamic electron correlation is properly accounted for. Similar findings have subsequently emerged at various levels of theory for a variety of rPSB models.<sup>11,16–21</sup> A remarkable study by Valsson et al. has shown that at the CASPT2 level of theory, torsional relaxation in PSB4 (a four-double bond model of rPSB) occurs along a single bond rather than a double bond and does not reach a CI.<sup>20</sup> Earlier, Send et al. had also demonstrated that protonated Schiff bases exhibit low or vanishing torsional barriers for single bond rotation at both the TD-DFT and CC2 levels of theory.<sup>22</sup> These studies made it clear that dynamic electron correlation is important for a proper description of the  $S_1$  PES of PSB3.

In order to quantify these effects, we map the  $S_1$  PES at both the CASSCF and CASPT2 levels of theory. Therefore, the  $\text{MEP}_{\text{CIS}}$ ,  $\text{MEP}_{\text{TRANS}}$ , and CI seam paths were generated independently at both levels of theory, as described in the Methods section below, and then single-point MRCISD, MRCISD+Q, MRPT2, and EOM-CC energy calculations were performed along these paths. We found, thus expanding early studies<sup>8,11,14–22</sup> that dynamic electron correlation does indeed have an important effect on the topology of the  $S_1$  PES in PSB3 and point to its importance for a proper quantitative and qualitative description of the mechanism and dynamics of the PSB3 isomerization and, most likely, for those of higher homologues.

## METHODS

This section outlines how the three CASSCF and CASPT2  $S_1$  paths were generated and how the dynamic electron correlation was introduced by single point energy calculations.

**Reference Potential Energy Surfaces.** To prepare the reference PES, three paths have been generated at the CASSCF and CASPT2 levels of theory. All optimizations and MEP calculations employed the 6-31G\* basis set with Cartesian  $d$  polarization functions and with an active space of six electrons in six  $\pi$  orbitals (6-in-6). In the case of CASPT2 optimizations and MEPs, the IPEA parameter was kept at the default value of 0.25.<sup>23</sup> Note that all references to CASPT2 geometries and paths assume that the IPEA for these calculations is the default 0.25 value. However, when we discuss single point calculations along the reference paths, a tag will be used to indicate whether the calculation is performed without an IPEA shift (IPEA = 0) or with (IPEA = 0.25). CASPT2 optimizations and MEP calculations were performed with numerical gradients.

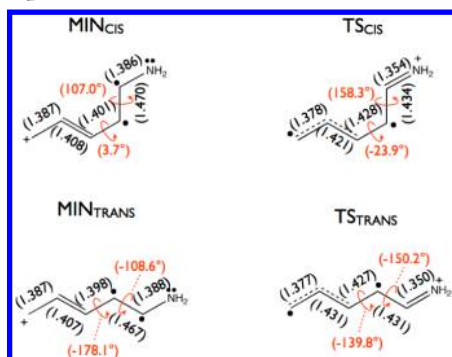
The first path,  $\text{MEP}_{\text{CIS}}$ , was generated for each of CASSCF and CASPT2 by an MEP calculation started from the *cis*-PSB3 Franck–Condon point optimized at the respective level of theory and with a radius of  $0.01 \text{ Å} \cdot (\text{amu})^{1/2}$  until a CI was reached (the CI intercepted by the  $\text{MEP}_{\text{CIS}}$  path will be called  $\text{CI}_{\text{CIS}}$ ). In the case of CASPT2, however, the MEP started from the FC point did not lead to a CI, as also reported by Valsson et al.<sup>20</sup> for a PSB4 model, but rather to a minimum ( $\text{MIN}_{\text{CIS}}$ ) reached by a twisting of the  $\text{C}_1-\text{C}_2$  single bond and a pyramidalization of the Schiff base nitrogen and  $\text{C}_1$  carbon. Therefore, a transition state ( $\text{TS}_{\text{CIS}}$ ) separating  $\text{MIN}_{\text{CIS}}$  from the CI had to be located by an  $S_1$  transition state optimization, and an MEP was launched in both the forward and backward directions from this transition state. The backward MEP eventually lead to the  $\text{MIN}_{\text{CIS}}$  structure, while the forward MEP lead to a  $\text{CI}_{\text{CIS}}$ . The three MEP calculations were combined into one continuous path (i.e., the CASPT2  $\text{MEP}_{\text{CIS}}$  path) which starts from the *cis*-PSB3 FC point, passes first through  $\text{MIN}_{\text{CIS}}$ , then rises to reach  $\text{TS}_{\text{CIS}}$ , and finally ends at  $\text{CI}_{\text{CIS}}$ .

The CASSCF and CASPT2  $\text{MEP}_{\text{TRANS}}$  paths were generated in exactly the same way as the CASSCF and CASPT2  $\text{MEP}_{\text{CIS}}$  paths, respectively, but starting from a *trans*-PSB3 structure optimized at the respective level of theory. The CASSCF  $\text{MEP}_{\text{TRANS}}$  path is barrierless and connects the *trans*-PSB3 FC point to  $\text{CI}_{\text{TRANS}}$  directly, while the CASPT2  $\text{MEP}_{\text{TRANS}}$  path encounters a  $\text{MIN}_{\text{TRANS}}$  structure and a  $\text{TS}_{\text{TRANS}}$  structure on the way. The structures of all  $S_1$  stationary points encountered by the CASPT2 paths are shown in Scheme 2.

In the case of the CASSCF  $\text{MEP}_{\text{CIS}}$  and  $\text{MEP}_{\text{TRANS}}$  paths, the first eleven structures were chosen to be  $0.01 \text{ Å} \cdot (\text{amu})^{1/2}$  apart, but then a structure was selected every  $0.02 \text{ Å} \cdot (\text{amu})^{1/2}$ . However, in the case of the CASPT2  $\text{MEP}_{\text{CIS}}$  and  $\text{MEP}_{\text{TRANS}}$  paths, the first nine structures were chosen to be  $0.01 \text{ Å} \cdot (\text{amu})^{1/2}$  apart, but then a structure was selected every  $0.08 \text{ Å} \cdot (\text{amu})^{1/2}$  from after the FC region up to the  $\text{TS}_{\text{CIS}}$  (in  $\text{MEP}_{\text{CIS}}$ ) or  $\text{TS}_{\text{TRANS}}$  (in  $\text{MEP}_{\text{TRANS}}$ ) structure. After the transition state, a point was selected every  $0.02 \text{ Å} \cdot (\text{amu})^{1/2}$  up to the point where the MEP intercepts a CI point.

Finally, the CI seam path was generated at each level of theory by a parabolic interpolation of internal coordinates using three structures. In the case of the CASSCF CI seam path, the three structures are the  $\text{CI}_{\text{CIS}}$  structure intercepted by the CASSCF  $\text{MEP}_{\text{CIS}}$  path, the  $\text{CI}_{\text{BLA}}$  structure which is the CI intercepted by the CASSCF BLA path of ref 8, and the  $\text{CI}_{\text{TRANS}}$  structure intercepted by the CASSCF  $\text{MEP}_{\text{TRANS}}$  path. As for the CASPT2 CI seam path, it is a parabolic interpolation of the  $\text{CI}_{\text{CIS}}$  structure intercepted by the CASPT2  $\text{MEP}_{\text{CIS}}$  path, the  $\text{CI}_{\text{BLA}}$  structure which is the CI intercepted by the CASPT2 (IPEA = 0.25) BLA path of ref 8, and the  $\text{CI}_{\text{TRANS}}$  structure

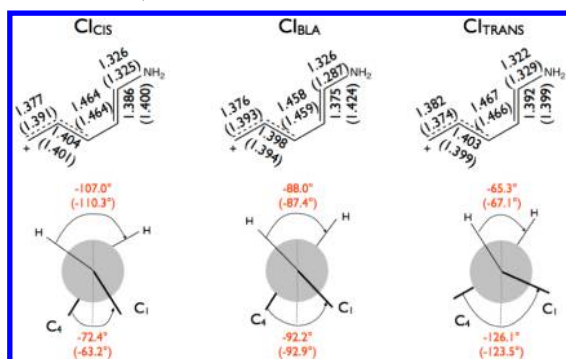
**Scheme 2. Structure of MIN<sub>CIS</sub>, MIN<sub>TRANS</sub>, TS<sub>CIS</sub>, and TS<sub>TRANS</sub> Optimized at the CASPT2 Level of Theory<sup>a</sup>**



<sup>a</sup>The bond-line formulas are a schematic representation of the dominant electronic configurations of the corresponding states. The geometry parameters are shown in parentheses. Bond length values are in angstroms and are displayed in black while torsions are displayed in red.

intercepted by the CASPT2 MEP<sub>TRANS</sub> path. Note that the “BLA path” of ref 8 is a path that follows a bond length alternation coordinate (which is the origin of the acronym BLA). The parabolic interpolation was done by fitting each internal coordinate with a polynomial fit to the second order and using the resulting equation to generate the interpolated internal coordinate values. The geometries of CI<sub>CIS</sub>, CI<sub>BLA</sub>, and CI<sub>TRANS</sub> which were used to generate the CI seam paths are shown in Scheme 3. Whereas the bond lengths are not very

**Scheme 3. Structures of CI<sub>CIS</sub>, CI<sub>BLA</sub>, and CI<sub>TRANS</sub> Used to Generate the CI Seam Path at the CASSCF and CASPT2 Levels of Theory<sup>a</sup>**



<sup>a</sup>The CASSCF and CASPT2 geometry parameters are shown (CASPT2 in parentheses). (top) Bond-line structures showing bond length values in angstroms. (bottom) Newman projection along the C2=C3 isomerizing bond. The the H—C2—C3—H and C1—C2—C3—C4 dihedrals are labeled.

different in the three CIs, their structures mainly differ along the hydrogen-out-of-plane (HOOP) coordinate. The HOOP (rigorously defined as the C1—C2—C3—C4 minus the H—C2—C3—H dihedral) is positive at CI<sub>CIS</sub>, almost zero at CI<sub>BLA</sub>, and negative at CI<sub>TRANS</sub>. However, the  $\pi$  orbital overlap ( $\tau$ , rigorously defined as the average of the two dihedrals involved in the HOOP) is almost 90° in all three cases, meaning that the  $\pi$  orbitals are orthogonal as would be expected at a CI.

Note that while the crossing points belonging to the computed CASSCF seam display the correct CI dimensionality (i.e. the degeneracy is lifted by distortion along two different

modes), this may not be the case for other theories (as reported in a different context in ref 24). For instance, at the MRCISD+Q level, the degeneracy is lifted only along the BLA mode since the Davidson correction corrects the energies but not the wavefunctions of the crossing states (and the CI is not truly “conical”). Nevertheless, throughout the manuscript, we will refer to the seam points as CI points.

**Multireference Configuration Interaction Calculations.** MRCISD and MRCISD+Q calculations were performed with Molpro<sup>25</sup> using the internally-contracted version.<sup>26</sup> The reference space employed the same electrons and orbitals as in the 6-in-6 active space used in CASSCF. The 1s core orbitals of carbon and nitrogen atoms were kept frozen. In MRCISD and MRCISD+Q calculations, as well as all other calculations throughout this work, the 6-31G\* basis set with Cartesian d polarization functions was used. In MRCISD+Q, the Davidson correction<sup>7</sup> with a relaxed reference<sup>27</sup> was used.

**Multireference Perturbation Theory Calculations.** The MRPT2 methods investigated in this work are CASPT2,<sup>28</sup> XMCQDPT2,<sup>29</sup> and NEVPT2.<sup>30,31</sup>

In the case of CASPT2, we investigate both single-state CASPT2 (hereon referred to as simply CASPT2) and multistate CASPT2 (MS-CASPT2),<sup>32</sup> both with and without the default IPEA parameter. CASSCF and CASPT2 energy calculations (as well as optimizations and MEP calculations discussed above) were all performed with the Molcas 7.8 quantum chemistry software package.<sup>33</sup> An imaginary shift of 0.2 was used in CASPT2 calculations to exclude intruder states.

The quasi-degenerate (QD-) formulation of NEVPT2 is used throughout this work. The reported QD-NEVPT2 energies are based on the partially contracted variant.<sup>34</sup>

XMCQDPT2 energies were computed using Firefly version 8.0.0.<sup>35</sup> In these calculations, the intruder state avoidance (ISA) shift was set to 0.02 to avoid intruder states. In addition to the classical version of XMCQDPT2, two more recently developed methods were also tested in this work (as in ref 8). The first, XMCQDPT2/diagonal fit, makes use of semicanonical orbitals obtained by block-diagonalization of a standard closed-shell-like canonical Fock operator built from the two-electron integrals and the first-order spin-free state-averaged CASSCF density matrix. Upon obtaining orbitals of different types, the energies of the active-space orbitals are redefined to provide the best possible one-particle least-squares approximation to the diagonal of the CASSCF Hamiltonian. The second, termed XMCQDPT2/F( $\Gamma_{ns}$ ), applies a modified Fock-like operator which incorporates some terms arising due to the nonseparable part ( $\Gamma_{ns}$ ) of the CASSCF state-averaged second-order density matrix  $\Gamma$ .

**Equation-of-Motion Coupled-Cluster Calculations.** In CCSD and EOM calculations, all electrons were correlated. Only the spin-flip (SF) variant of EOM<sup>36–39</sup> was tested due to its success in a previous benchmark study employing the PSB3 model.<sup>11</sup> The lowest high-spin triplet was employed as the reference, which was computed at the ROHF level of theory to reduce spin-contamination. In this work, we employ EOM-SF-CCSD (or, for brevity, SF-CCSD) and SF-CCSD(dT). The former includes only single and double substitutions, while the latter is augmented by a perturbative triples correction obtained by using second-order Rayleigh–Schrödinger perturbation theory.<sup>40</sup> In SF-CCSD(dT), the diagonal of the full similarity transformed Hamiltonian is employed. All EOM-SF calculations were performed using the Q-Chem electronic structure package.<sup>41</sup>



**Charge Transfer Character.** In the following, we probe the electronic character of PSB3 by looking at the charge transfer character across the C2=C3 bond. The charge transfer character across the C2=C3 bond for a certain geometry is computed as the sum of the charges of all the atoms in the allyl ( $\text{C}_5\text{H}_2=\text{C}_4\text{H}-\text{C}_3\text{H}=\text{C}_2\text{H}=\text{C}_1\text{H}$ ) moiety of PSB3. The charge transfer character across the C1—C2 bond is computed by taking the sum of the charges on the  $-\text{C}_2\text{H}=\text{C}_3\text{H}-\text{C}_4\text{H}=\text{C}_5\text{H}_2$  moiety of PSB3. These charge transfer characters are computed at both the CASSCF and CASPT2 levels of theory using Mulliken population analysis performed by Molcas.<sup>33</sup>

**Nonparallelity Errors.** In the Results and Discussion section, we present and discuss nonparallelity errors (NPEs). NPEs are useful for quantitatively comparing different methods along a potential energy path. They are computed by finding the energy deviation of each point along the path from the reference method (in our case taken to be MRCISD+Q) and then subtracting the minimum deviation from the maximum deviation. A large NPE generally indicates that a method differentially treats different regions of the PES; whereas, a small NPE indicates that the potential energy computed at that level of theory is parallel to that of the reference method along the path of interest.

## RESULTS AND DISCUSSION

In the following section, we analyze the CASSCF and CASPT2 reference paths and then present the results for MRCISD, MRCISD+Q, MRPT2, and EOM-CC energy corrections on the two surfaces.

**Analysis of Reference Potential Energy Surfaces.** The energy profile along the composite reaction path, comprising the  $\text{MEP}_{\text{CIS}}$ , CI seam, and  $\text{MEP}_{\text{TRANS}}$  paths, is shown in Figure 1 for the CASSCF and CASPT2 levels of theory. There are several differences between the CASSCF and CASPT2 paths, as highlighted above. Most notably, the molecule at the CASSCF level isomerizes immediately around the C2=C3 double bond, whereas with at the CASPT2 level it follows a barrierless but very shallow path along a C1—C2 single bond isomerization coordinate, with a barrier along the C2=C3 double bond which needs to be overcome to lead to *cis*–*trans* isomerization. Notice that the  $\text{MIN}_{\text{CIS}}$  and  $\text{MIN}_{\text{TRANS}}$  structures occupy a very flat region of the  $\text{S}_1$  PES.

At the FC point of *cis*-PSB3 and *trans*-PSB3, there is steep decrease in energy in the  $\text{S}_1$  state (and a corresponding rise in energy in the  $\text{S}_0$  state). This sudden change in energy in the FC regions is associated with a large change of bond length alternation (BLA) associated with an increase in double-bond lengths and decrease in single bond lengths (see Figure 2A). This phenomenon has been well documented in rPSB and its models.<sup>13,42–44</sup> We find that this initial relaxation along the BLA coordinate is predicted by both CASSCF and CASPT2 but is much more pronounced in CASSCF where the decrease in BLA is on the order of 0.15 Å and the associated change in energy is ca. 10 kcal/mol (compared to CASPT2 that has a BLA decrease of 0.04 Å and an associated energy change of ~5 kcal/mol). In both cases, the large change in BLA is accompanied by a very limited increase in charge transfer character with respect to the reactive C2=C3 bond (see Figure 2B).

This difference in BLA behavior of CASSCF and CASPT2 near the FC point arises due to the existence of a so-called “locally excited” (LE) region on the CASPT2  $\text{S}_1$  PES. Such a region has been recently documented in a hybrid quantum

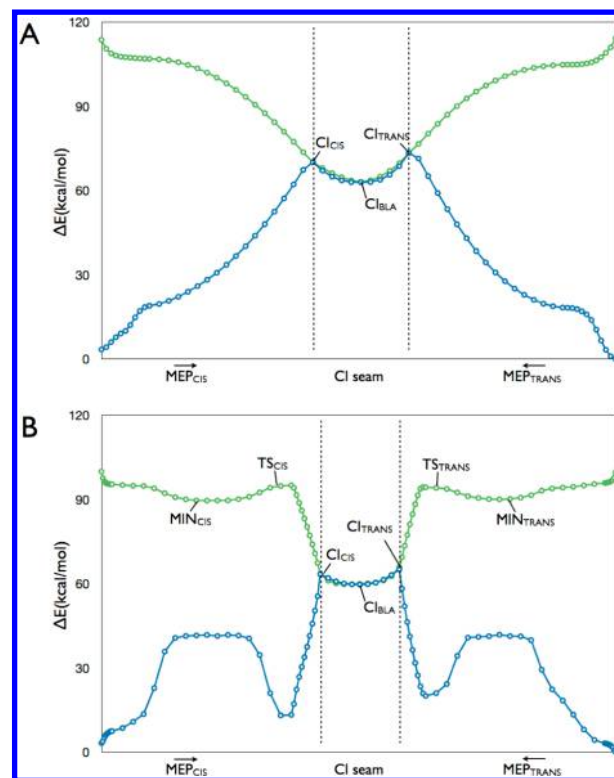


**Figure 1.**  $\text{S}_0$  (blue) and  $\text{S}_1$  (green) energy profiles along the composite CASSCF (A) and CASPT2 (B) paths comprising the  $\text{MEP}_{\text{CIS}}$ , CI seam, and  $\text{MEP}_{\text{TRANS}}$  paths (the three paths are separated by dashed vertical lines). The points corresponding to the structures shown in Schemes 2 and 3 are labeled in the graph. Energies are relative to the *trans*-PSB3  $\text{S}_0$  energy and are reported at the respective level of theory at which the geometries were generated.

mechanics/molecular mechanics (QM/MM) model of bovine rhodopsin incorporating a rPSB chromophore with the isomerizing double bond locked in a 5-membered ring.<sup>45</sup> In this work, it has been proposed that the LE region hosts an  $\text{S}_1$  intermediate from which fluorescence may occur, or which may lead to an alternate decay pathway for the  $\text{S}_1$  population (i.e., other than the double-bond isomerization mechanism). An LE region has also been located in a QM/MM model<sup>46</sup> of a member of a recently engineered set of rhodopsin mimics based on mutated cellular retinoic acid binding proteins.<sup>47–49</sup> Finally, such a region has also been located along a CASPT2 relaxed scan for PSB3.<sup>46</sup>

At the CI seam, we see a marked difference in the BLA profile of Figure 2A between CASSCF and CASPT2. Indeed, the BLA along the interpolation coordinate in that region has positive curvature at the CASSCF level and negative at the CASPT2 level. This is due to the fact that while  $\text{CI}_{\text{CIS}}$  and  $\text{CI}_{\text{TRANS}}$  have similar BLA values at the CASSCF and CASPT2 levels of theory,  $\text{CI}_{\text{BLA}}$  is different for each method (with a BLA value of ca. 0 and 0.3 Å for CASSCF and CASPT2, respectively) causing the CI seam profile to be different. As expected, along the CASSCF path, the two states appear to have mixed character along most of the CI seam. As shown in Figure 2B, the charge transfer character remains at almost 0.5  $e^-$  for both  $\text{S}_0$  and  $\text{S}_1$ . This indicates that both states have a mixed electronic character that is in between that of a full charge-transfer and diradical configuration. There are sudden changes in the charge transfer character along the CASSCF CI seam due to the near degeneracy situation.<sup>50</sup>

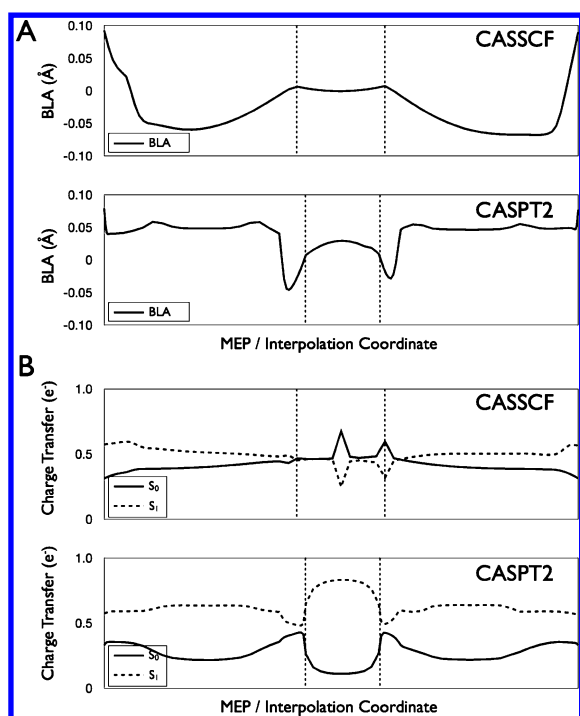


**Figure 2.** (A) BLA value along the CASSCF (top) and CASPT2 (bottom) composite paths. The dashed vertical lines are used to distinguish the three paths: (from left to right)  $\text{MEP}_{\text{CIS}}$ , CI seam, and  $\text{MEP}_{\text{TRANS}}$ . The BLA value is computed as the difference between the average bond length of single bonds and double bonds along the PSB3 backbone. (B) Charge transfer character across the  $\text{C2}=\text{C3}$  bond along the CASSCF and CASPT2 composite paths.

Along the CASPT2 CI seam, the geometries have a complete charge transfer character on  $S_1$  (accompanied by a completely diradical  $S_0$  character). Technically this can be explained by the increase in BLA with respect to the CASSCF CI seam, which brings the molecule into charge transfer region on  $S_1$  in the underlying CASSCF level of theory where the states are no longer degenerate. This charge transfer region is characterized by large twisting about the  $\text{C2}=\text{C3}$  double bond, and an electronic structure consistent with that of a twisted intramolecular charge transfer (TICT)<sup>51,52</sup> state reaching top charge separation at  $\text{CI}_{\text{BLA}}$  with a ca.  $90^\circ$   $\text{C1}-\text{C2}-\text{C3}-\text{C4}$  dihedral angle and a ca.  $0^\circ$  HOOP. As reported in previous work, such TICT character may also develop along paths and trajectories approaching the seam.<sup>53</sup> In such cases, a sudden polarization effect<sup>54</sup> is expected when along the path the charge transfer suddenly rises from ca. 0.5 to 1.0.

Figure 3A displays the dihedral angles related to the double bond isomerization along the CASSCF and CASPT2 paths. We find that near the FC regions of *cis*-PSB3 and *trans*-PSB3 there is little torsional change due to the initial relaxation from the FC being dominated by a BLA mode. As discussed in the methods section, in the case of CASSCF isomerization of the double bond begins immediately and leads to a CI, whereas for CASPT2 the double bond isomerization does not occur until later in the  $\text{MEP}_{\text{CIS}}$  and  $\text{MEP}_{\text{TRANS}}$  coordinates. A comparison of Figures 2A and 3A reveals a relation between the BLA coordinate and the isomerization. At (or just before) the start of the isomerization, the BLA value decreases rapidly, reaches a minimum, and then increases again as twisting occurs until a CI is reached. This trend in BLA is observed in both CASSCF and

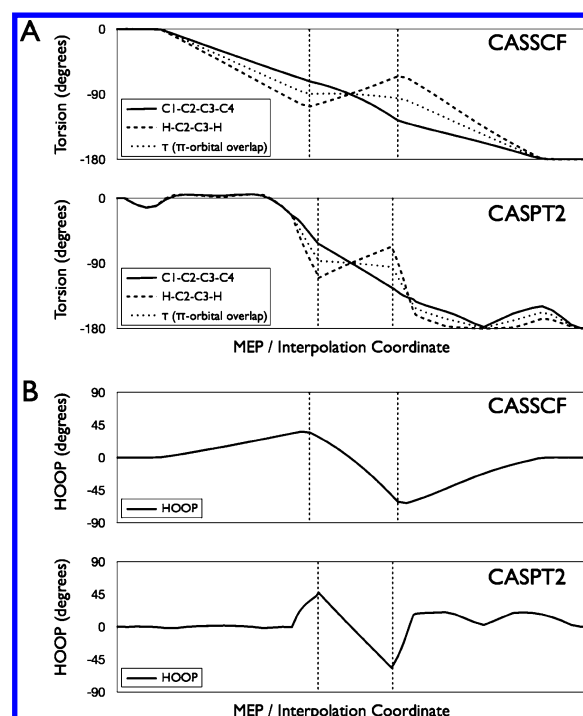


**Figure 3.** (A) The  $\text{C1}-\text{C2}-\text{C3}-\text{C4}$ ,  $\text{H}-\text{C2}-\text{C3}-\text{H}$  dihedrals and  $\pi$ -orbital overlap ( $\tau$ , calculated as the average of the  $\text{C1}-\text{C2}-\text{C3}-\text{C4}$  and  $\text{H}-\text{C2}-\text{C3}-\text{H}$  dihedrals) along the CASSCF (top) and CASPT2 (bottom) composite paths. The dashed vertical lines are used to distinguish the three paths: (from left to right)  $\text{MEP}_{\text{CIS}}$ , CI seam, and  $\text{MEP}_{\text{TRANS}}$ . (B) Hydrogen-out-of-plane (HOOP, defined as the difference between the  $\text{C1}-\text{C2}-\text{C3}-\text{C4}$  and  $\text{H}-\text{C2}-\text{C3}-\text{H}$  dihedrals) along the CASSCF (top) and CASPT2 (bottom) composite paths.

CASPT2 (although in CASSCF the onset is earlier than in CASPT2)

The role of HOOP in the isomerization of rPSB in visual pigments has been documented in several QM/MM trajectory calculations.<sup>53,55</sup> Here, we see that the HOOP mode is largely involved in the isomerization even in a MEP calculation of a gas-phase PSB3 model (Figure 3B). Its involvement is thus not due to dynamics reasons exclusively, but, mainly, to the actual  $S_1$  force field. The  $\text{C1}-\text{C2}-\text{C3}-\text{C4}$  dihedral is coupled with an even larger change in  $\text{H}-\text{C2}-\text{C3}-\text{H}$  dihedral in both  $\text{MEP}_{\text{CIS}}$  and  $\text{MEP}_{\text{TRANS}}$ , and, therefore, the absolute value of the HOOP increases from  $0^\circ$  at the FC points to  $30$ – $60^\circ$  at the CI. Note that isomerization starting from *cis*-PSB3 leads to a positive value of HOOP, favoring isomerization to *trans*-PSB3, while starting from *trans*-PSB3 yields a negative HOOP, favoring isomerization to *cis*-PSB3. Therefore, the  $\text{CI}_{\text{CIS}}$  and  $\text{CI}_{\text{TRANS}}$  have completely opposite HOOP values, and the path along the CI seam is dominated by a change in the HOOP coordinate (Figure 3B). Meanwhile, the  $\pi$ -orbital overlap (represented by the geometrical variable  $\tau$ , defined in the Figure 3 caption) remains almost constant along the CI seam (Figure 3A). Interestingly, we find that the  $\text{CI}_{\text{TRANS}}$  has a larger absolute HOOP value than  $\text{CI}_{\text{CIS}}$  at both the CASSCF ( $\text{CI}_{\text{TRANS}}$  is  $-60.8^\circ$  and  $\text{CI}_{\text{CIS}}$  is  $34.6^\circ$ ) and CASPT2 ( $\text{CI}_{\text{TRANS}}$  is  $-56.4^\circ$  and  $\text{CI}_{\text{CIS}}$  is  $47.1^\circ$ ) levels of theory.

In Figure 4A, we find that while CASSCF displays virtually no change in the  $\text{N}-\text{C1}-\text{C2}-\text{C3}$  dihedral along  $\text{MEP}_{\text{CIS}}$  and  $\text{MEP}_{\text{TRANS}}$ , at the CASPT2 level of theory isomerization around the  $\text{C1}-\text{C2}$  single bond starts to occur almost immediately

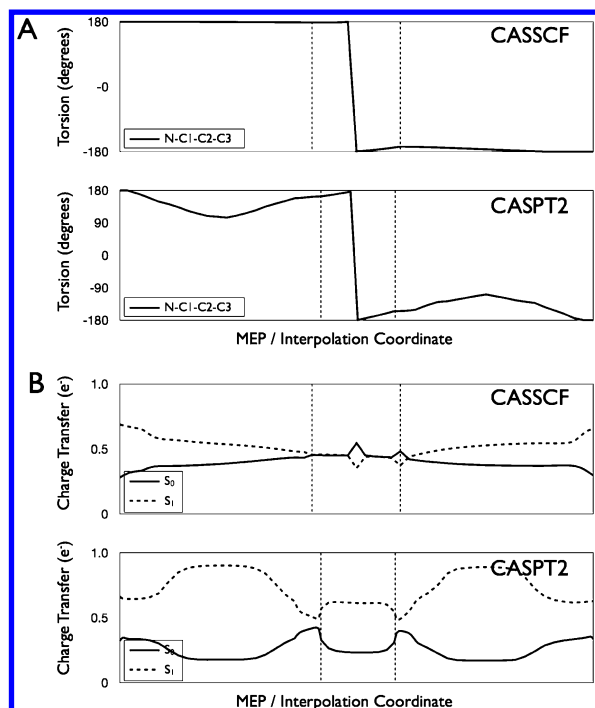


**Figure 4.** (A) N–C1–C2–C3 dihedral along the CASSCF (top) and CASPT2 (bottom) composite paths. The dashed vertical lines are used to distinguish the three paths: (from left to right) MEP<sub>CIS</sub>, CI seam, and MEP<sub>TRANS</sub>. (B) Charge transfer character across the C1–C2 bond along the CASSCF and CASPT2 composite paths.

from the FC point (after just a small relaxation in the BLA shown in Figure 2A bottom). This isomerization leads to an S<sub>1</sub> minimum that is  $\sim 70^\circ$  twisted with respect to the FC point (MIN<sub>CIS</sub> or MIN<sub>TRANS</sub>). This single bond isomerization is associated with a very limited change in the BLA (Figure 2A bottom), but with a significant charge transfer across the C1–C2 bond such that the molecule has the positive charge almost fully localized on the  $-C_2H=C_3H-C_4H=C_5H_2$  moiety (Figure 4B bottom). Therefore, the MIN<sub>CIS</sub> or MIN<sub>TRANS</sub> structures may be seen as single-bond TICT states corresponding to real and, in principle, fluorescent S<sub>1</sub> intermediates. Finally, we find from a comparison of Figures 3A and 4A that along MEP<sub>CIS</sub> the single bond and double bond isomerizations are almost independent (the dihedral around the C2=C3 double bond remains planar while single bond isomerization occurs), but the same is not true for MEP<sub>TRANS</sub>. This last observation is also related to the fact that TS<sub>TRANS</sub> has a larger torsional deformation in both the C1–C2 single and C2=C3 double bond than TS<sub>CIS</sub>.

In summary, we found several differences between the CASSCF and CASPT2 paths. The main difference along the MEP<sub>CIS</sub> and MEP<sub>TRANS</sub> paths is the existence of a LE region on the S<sub>1</sub> CASPT2 PES of PSB3 near the FC point which is absent in CASSCF. This corresponds to a difference in topology of the potential energy surface and is, therefore, of mechanistic significance. Such a region must have a significant effect on the initial relaxation dynamics along the BLA coordinate from the FC point, as observed in several studies.<sup>14,19,20</sup> However, it is noteworthy to mention that even along the CASPT2 path the BLA does decrease significantly, as in CASSCF, once the molecule leaves the LE region. The LE region in CASPT2 also introduces an S<sub>1</sub> barrier for isomerization along the C2=C3 double bond, instead favoring a torsional deformation along the

C1–C2 single bond. As mentioned above, this is consistent with what was found by Valsson et al.<sup>20</sup> and Send et al.<sup>22</sup> in different rPSB models. However, it is important to stress that such single bond deformation does not lead to a degeneracy of the S<sub>1</sub> and S<sub>0</sub> states and may be considered photochemically (but not photophysically) of a limited importance. Indeed, note that a removal of the path segments dominated by single bond deformation from the energy profile of Figure 1B would produce, after splicing the remaining segments, composite CASPT2 energy profiles topologically similar to the CASSCF profiles of Figure 1A. Finally, we find that differences in the CI structures at the CASSCF and CASPT2 level (and especially in the CI<sub>BLA</sub> structure) leads to a different shape of the CI seam at the two levels of theory.

**Dynamic Electron Correlation Effects on the CASSCF Reference PES.** In this section, we perform MRCI, MRPT2, and EOM-CC single point calculations along the composite CASSCF path comprising MEP<sub>CIS</sub>, CI seam, and MEP<sub>TRANS</sub>. Figure 5 displays the energy profiles along the composite path

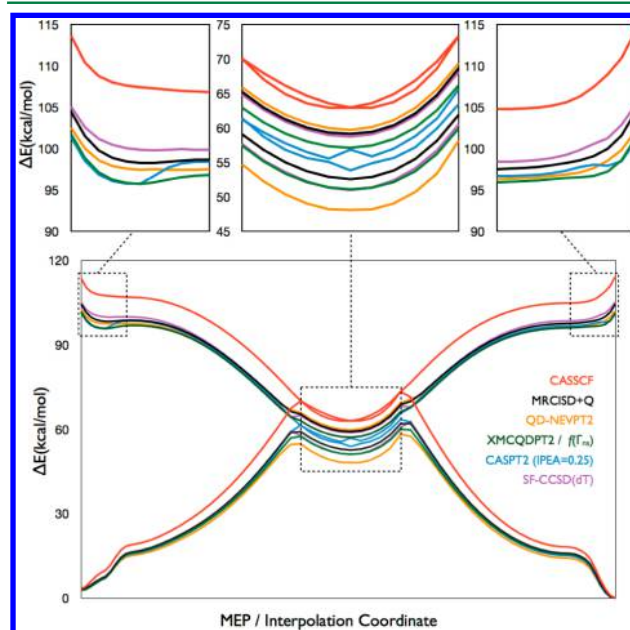


**Figure 5.** CASSCF (red), MRCISD+Q (black), QD-NEVPT2 (orange), XMCQDPT2/F(Γ<sub>ns</sub>) (green), CASPT2 (IPEA = 0.25) (blue), and SF-CCSD(dT) (violet) energy profiles along the composite CASSCF path comprising MEP<sub>CIS</sub>, CI seam, and MEP<sub>TRANS</sub>. The energies are relative to the *trans*-PSB3 S<sub>0</sub> energy. The insets show an expansion of the 10 points nearest to each of the *cis*- and *trans*-PSB3 structures and of the CI seam.

(we display only one variant of each method that performs better than the rest. For figures including all tested methods please see Figures S1 and S2 in the Supporting Information, SI). We find that dynamic electron correlation stabilizes the S<sub>1</sub> state along the entire path and, also, stabilizes the S<sub>0</sub> energy of all structures relative to the equilibrium *cis*- and *trans*-PSB3 structures. Near the *cis*-PSB3 and *trans*-PSB3 FC regions (see left and right insets in Figure 5), we notice that the clearly barrierless CASSCF S<sub>1</sub> path becomes flatter upon introduction of dynamic electron correlation or even develops an S<sub>1</sub> barrier, forming a minimum. This is most noticeable at the CASPT2 (IPEA = 0.25) level of theory, but the effect is present with other MRPT2, MRCISD+Q, and EOM-CC methods as well.



**Table 1.**  $S_0$ – $S_1$  Energy Gaps ( $\Delta E_{S_0-S_1}$ ) at *cis*-PSB3, *trans*-PSB3,  $CI_{CIS}$ ,  $CI_{BLA}$ , and  $CI_{TRANS}$ , as well as the NPEs for Various Methods along the Composite (Full) CASSCF Path<sup>a</sup>

method	$\Delta E_{S_0-S_1}$ at <i>cis</i> -PSB3	$\Delta E_{S_0-S_1}$ at <i>trans</i> -PSB3	$\Delta E_{S_0-S_1}$ at $CI_{CIS}$	$\Delta E_{S_0-S_1}$ at $CI_{BLA}$	$\Delta E_{S_0-S_1}$ at $CI_{TRANS}$	composite path $S_0$ NPE	composite path $S_1$ NPE	CI seam $S_0$ NPE	CI seam $S_1$ NPE
MRCISD+Q	<i>101.4</i>	<i>104.4</i>	6.2	6.6	6.8	<i>0.0</i>	<i>0.0</i>	<i>0.0</i>	<i>0.0</i>
MRCISD	104.8	108.1	4.6	4.9	5.0	4.5	1.9	0.7	0.5
CASSCF	<b>110.3</b>	<b>114.1</b>	<b>0.0</b>	<b>0.0</b>	<b>0.0</b>	<b>11.4</b>	<b>6.0</b>	<b>1.6</b>	<b>1.2</b>
XMCQDPT2	94.4	96.6	3.0	3.5	3.7	3.1	3.3	0.3	0.4
XMCQDPT2/ diagonal fit	100.9	103.3	6.1	6.5	6.9	3.9	2.5	0.5	0.3
XMCQDPT2/ $F(\Gamma_{ns})$	99.0	101.2	5.5	6.0	6.2	2.3	1.9	0.5	0.5
QD-NEVPT2	99.4	102.1	11.2	11.6	11.2	4.8	3.1	1.0	0.3
CASPT2 (IPEA = 0)	92.0	94.4	0.4	0.0	0.1	3.0	5.3	1.0	0.7
MS-CASPT2 (IPEA = 0)	92.5	95.0	17.2	16.4	17.4	9.2	11.8	1.3	0.5
CASPT2 (IPEA = 0.25)	98.2	100.9	−0.2	3.0	2.2	3.3	3.8	1.0	1.7
MS-CASPT2 (IPEA = 0.25)	98.5	101.3	15.9	15.2	16.1	5.8	7.6	1.0	0.5
SF-CCSD	105.5	109.3	2.2	2.7	0.5	2.6	8.7	0.3	0.3
SF-CCSD(dT)	102.1	105.2	7.2	7.8	7.6	2.3	3.6	0.2	0.2

<sup>a</sup>All values are reported in kilocalories per mole. NPEs were computed along the composite (full) path which combines  $MEP_{CIS}$ , the CI seam, and  $MEP_{TRANS}$ , as well as just along the CI seam. The reference values (i.e. MRCISD+Q) are highlighted in italic font, while the values obtained at the level of theory with which the paths were generated are highlighted in bold.

Along the CI seam (Figure 5, center inset), we notice that dynamic electron correlation lifts the degeneracy between the  $S_0$  and  $S_1$  states along the seam (to a different degree depending on the method). The only exception is CASPT2 (IPEA = 0.25) where the  $S_0$  and  $S_1$  states remain degenerate along the seam, except at  $CI_{BLA}$  where the degeneracy splits suddenly. This behavior of CASPT2 (IPEA = 0.25) can be explained by looking at the electronic character of the underlying CASSCF wave function shown in the top of Figure 2B. We find that the  $S_0$  and  $S_1$  wave functions are strongly mixed along this path, except near  $CI_{BLA}$  (and a little also near  $CI_{TRANS}$ ) where we see sudden variations in the wave function. Due to an already documented problematic behavior of CASPT2,<sup>8,29</sup> these variations in the CASSCF wave function near a CI can result in sudden variations of the CASPT2 energy, resulting in artifacts such as those observed here. In fact, the MS-CASPT2 (IPEA = 0.25) profile is significantly different along the CI seam (see Figure S2 in the SI), leading to an overestimation of the energy gap (as also documented in ref 8).

In order to more accurately compare the different methods, we present in Table 1 a more quantitative analysis of their performance along the composite CASSCF path. Namely, we present the  $S_0$ – $S_1$  energy gaps ( $\Delta E_{S_0-S_1}$ ) at the equilibrium structures and the CI structures used to construct the CI seam. We also report NPEs along the composite path and the CI seam. It may be useful to compare this table with the profiles of Figure 5 and Figures S1 and S2 in the SI. MRCISD+Q is considered here to be the most accurate method and, therefore, is the reference against which NPEs are computed and to which energy gaps are compared.

We will now discuss the energy gaps at the *cis*- and *trans*-PSB3 geometries. MRCISD+Q has energy gaps (101.4 and 104.4 kcal/mol for *cis*- and *trans*-PSB3, respectively) that are ca. 9–10 kcal/mol smaller than those of CASSCF. In fact, we find that dynamic electron correlation consistently reduces the energy gap at the equilibrium structures. While MRCISD without the Davidson correction and EOM-CC methods give larger energy gaps than MRCISD+Q, all MRPT2 methods

underestimate them. In the case of XMCQDPT2, while the classical version gives energy gaps that are 7–8 kcal/mol smaller than MRCISD+Q, the diagonal fit and  $F(\Gamma_{ns})$  variants yield a very good (and in the case of diagonal fit – excellent) agreement with MRCISD+Q. QD-NEVPT2 also performs very well in reproducing the MRCISD+Q energy gaps. As for CASPT2 and MS-CASPT2, we find that the energy gaps computed without the IPEA shift are largely red-shifted by 9–10 kcal/mol, but the introduction of the IPEA shift significantly improves the agreement with MRCISD+Q. Both with and without the IPEA shift, MS-CASPT2 performs slightly better than CASPT2. We note that the effect of the IPEA, as well as the basis set and geometry optimization, was already explored in our previous benchmark addressing the ground state PES.<sup>8</sup> In that study, it was found that for *cis*- and *trans*-PSB3, when a modest (6-31G\*) basis set is used with a CASSCF optimized geometry, it appears to be more accurate to use CASPT2 without an IPEA shift rather than with the default IPEA, as this allows for better agreement due to a cancellation of errors (including differences in optimized geometries, IPEA values and modest basis sets). This cancellation, if general, may be important for cases where large basis sets and CASPT2 optimizations may not be affordable. Finally, we notice in Table 1 that SF-CCSD with the triples correction (dT) reproduces the MRCISD+Q energy gaps very well.

From the energy gaps at the  $CI_{CIS}$ ,  $CI_{BLA}$ , and  $CI_{TRANS}$  geometries, we find that MRCISD+Q splits the degeneracy that exists at the CASSCF level of theory at these structures, as we already saw in Figure 5 along the entire CI seam. The degree of splitting of the degeneracy is different for different methods. This is due to CI being displaced to different geometries along the BLA coordinate, as already documented in ref 8. At the XMCQDPT2 level, the energy splitting at the three CI geometries is in reasonable agreement with MRCISD+Q, especially when the diagonal fit and  $F(\Gamma_{ns})$  variants are used. QD-NEVPT2 overestimates the energy gap by ca. 4–5 kcal/mol. This is due to the overstabilization of the  $S_0$  energy in that region of the PES, a property of QD-NEVPT2 that has already

been documented in several works<sup>8,56</sup> and was found to be due to the limit in the zero-order CASSCF wave function. This issue could be resolved by using a larger active space for the underlying CASSCF wave function.<sup>8,56</sup> In the case of CASPT2, we find that these CI structures present a particular challenge due to the degeneracy of the CASSCF  $S_0$  and  $S_1$  states and strong mixing of the corresponding wave functions. As a result, we notice that two states remain almost degenerate along the entire CI seam at the CASPT2 (IPEA = 0) level, as well as with the CASPT2 (IPEA = 0.25) level (especially at  $CI_{CIS}$  where the mixing of states is largest (Figure 2B top)). This artifact also leads to a large overestimation of the energy gaps at the MS-CASPT2 (IPEA = 0) and MS-CASPT2 (IPEA = 0.25) levels of theory as the available implementations overcorrect for the artifactual degeneracy.<sup>8,29</sup> Finally, we notice that while the energy gap at the CI structures remains small with SF-CCSD, the triples correction again improves the agreement with MRCISD+Q.

The NPE values provide a good indication of the overall performance of each method along the composite CASSCF path. We also present in Table 1 the NPE value along just the CI seam, since this region may be of particular interest to the photochemistry of the system. In fact, a low NPE would imply that the CI seam has the same shape along the PES, but is displaced to a different region (e.g., could be displaced along the BLA value). On the other hand, a large NPE would indicate that the shape of the CI seam changes with the method, and therefore, this would indicate a different dependence of the energy gap on the geometrical coordinates. In fact, we find from Table 1 that the NPE values along the CASSCF CI seam are very small, confirming that CI seams computed at one level of theory have a reasonably correct shape, at least in the case of PSB3. The largest NPE value observed is for CASSCF, but this value is still not significantly large. This is followed by CASPT2 and MS-CASPT2, but this can be easily explained by artifacts along the CI seam region arising from the variations in the underlying CASSCF wave functions, especially at  $CI_{BLA}$  and  $CI_{TRANS}$ . Also, for QD-NEVPT2, while the NPE for the  $S_1$  state is very small, it is larger for  $S_0$ . Again, this could possibly be remedied by improving the zero-order CASSCF wave function (i.e., expanding the active space).

Along the composite CASSCF path, we naturally start to see larger NPE values, indicating that there are fewer methods capable of describing the full path. For example, along the CASSCF path we find NPE values of 11.4 and 6.0 kcal/mol for the  $S_0$  and  $S_1$  states, respectively. The effect is large enough to be visibly seen in Figure 5, where we find that the MRCISD+Q profiles along both the  $S_0$  and  $S_1$  states are significantly flatter than those of CASSCF. On the other hand, XMCQDPT2 displays a relatively negligible NPE for both  $S_0$  and  $S_1$  along the path, in particular with the  $F(\Gamma_{ns})$  variant which performs remarkably well relative to MRCISD+Q. QD-NEVPT2 has a larger NPE value than XMCQDPT2, but this is mainly due to the CI seam region where it deviated from the MRCISD+Q CI seam. If we ignore the CI seam and two nearby structures from each side of the seam, we would obtain an NPE of 3.0 kcal/mol for  $S_0$  and 1.7 kcal/mol for  $S_1$ . This means that QD-NEVPT2 is able to describe most of the PSB3 PES mapped in this work and only suffers from overstabilizing one of the states when the molecule is completely twisted (particularly, the state with charge transfer character as documented in our previous benchmark study<sup>8</sup>). We also see a reasonably good NPE value for CASPT2. The IPEA shift has small effect on the NPE value,

indicating that the shift only moves up the entire PES, but does not change its topology significantly. However, MS-CASPT2 displays very large NPEs, comparable with CASSCF, but this is again due to the CI seam region where artifacts occur and cause a large splitting in the energy degeneracy. In fact, if the CI seam and nearby regions were ignored when computing the NPEs, the NPE value would decrease. Finally, while SF-CCSD has a relatively large NPE value (especially for the  $S_1$  state), the triples correction significantly improves the agreement with MRCISD+Q. In Figure 5, we notice that along most of the path SF-CCSD(dT) remains very close to the MRCISD+Q curve.

**Dynamic Electron Correlation Effects on the CASPT2 Reference PES.** In Figure 6, we present the energy profiles for

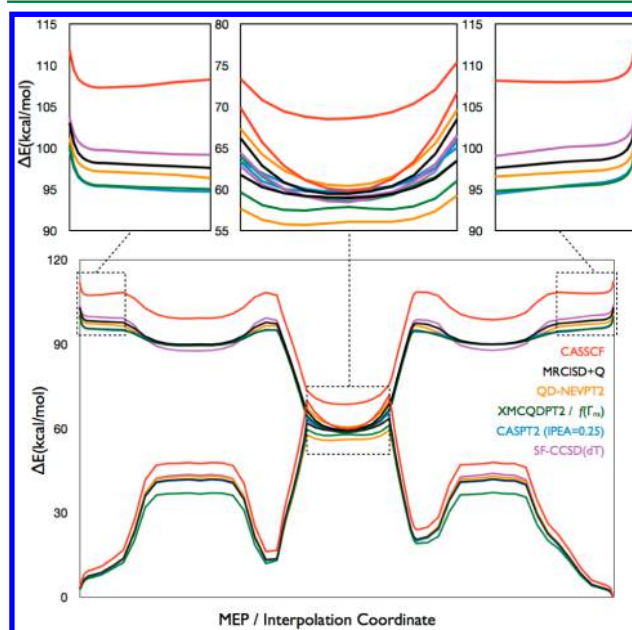


**Figure 6.** CASSCF (red), MRCISD+Q (black), QD-NEVPT2 (orange), XMCQDPT2/ $F(\Gamma_{ns})$  (green), CASPT2 (IPEA = 0.25) (blue), and SF-CCSD(dT) (violet) energy profiles along the composite CASPT2 (IPEA = 0.25) path comprising  $MEP_{CIS}$ , CI seam, and  $MEP_{TRANS}$ . The energies are relative to the *trans*-PSB3  $S_0$  energy. The insets show an expansion of the 12 points nearest to each of the *cis*- and *trans*-PSB3 structures and of the CI seam.

several methods along the composite CASPT2 (IPEA = 0.25) path (the same methods presented in Figure 5; all other methods are shown in Figures S3 and S4 in the SI). There are several notable differences between Figures 5 and 6. First, we find that all methods display a barrierless path along the single bond isomerization, with the exception of CASSCF (see left and right insets in Figure 6). Therefore, while CASSCF predicts a completely barrierless double bond isomerization and a barrier along the single bond isomerization, correlated methods display a barrierless single bond isomerization instead. Therefore PSB3 presents an interesting example of a system where single and double bond isomerizations are both possible on  $S_1$  and different methodologies may predict a different reactivity. On the other hand, it should be stressed again that the nonadiabatic reaction leading to double bond isomerization is qualitatively invariant and displays the same mechanistic features (i.e., a BLA change precedes the torsional motion typical of a two-states two-modes mechanism) for both the CASSCF and CASPT2 levels. In contrast the single bond conformational change (i.e., an *s-trans* to *s-cis* change) is an



**Table 2.**  $S_0$ – $S_1$  Energy Gaps ( $\Delta E_{S_0-S_1}$ ) at  $\text{MIN}_{\text{CIS}}$ ,  $\text{MIN}_{\text{TRANS}}$ ,  $\text{CI}_{\text{CIS}}$ ,  $\text{CI}_{\text{BLA}}$ , and  $\text{CI}_{\text{TRANS}}$ , as well as  $\text{TS}_{\text{CIS}}$  and  $\text{TS}_{\text{TRANS}}$  Energy Barriers and NPEs for Various Methods along the Composite (Full) CASPT2 Path<sup>a</sup>

method	$\Delta E_{S_0-S_1}$ at $\text{MIN}_{\text{CIS}}$	$\Delta E_{S_0-S_1}$ at $\text{MIN}_{\text{TRANS}}$	$\text{TS}_{\text{CIS}}$ barrier	$\text{TS}_{\text{TRANS}}$ barrier	$\Delta E_{S_0-S_1}$ at $\text{CI}_{\text{CIS}}$	$\Delta E_{S_0-S_1}$ at $\text{CI}_{\text{BLA}}$	$\Delta E_{S_0-S_1}$ at $\text{CI}_{\text{TRANS}}$	full path $S_0$ NPE	full path $S_1$ NPE	CI seam $S_0$ NPE	CI seam $S_1$ NPE
MRCISD+Q	47.9	47.9	7.4	7.1	4.4	0.5	5.0	0.0	0.0	0.0	0.0
MRCISD	48.9	48.8	7.9	8.0	4.0	2.8	4.4	3.7	1.8	2.6	0.3
CASSCF	51.3	50.7	8.3	9.1	3.5	8.7	3.7	8.2	4.6	7.4	2.2
XMCQDPT2	48.4	48.7	3.1	2.9	2.8	3.0	3.6	4.3	6.2	1.4	2.8
XMCQDPT2/ diagonal fit	51.4	51.8	5.1	4.6	4.9	0.3	5.6	3.8	4.1	1.1	0.6
XMCQDPT2/ $F(\Gamma_{\text{ns}})$	52.4	52.6	5.5	5.0	4.8	0.6	5.5	4.9	3.1	1.3	1.2
QD-NEVPT2	46.5	46.9	6.9	6.5	9.7	4.4	10.3	5.3	3.6	1.3	0.5
CASPT2 (IPEA = 0)	44.2	44.6	3.0	2.1	3.0	5.1	3.6	4.0	10.7	1.3	4.8
MS-CASPT2 (IPEA = 0)	44.2	44.6	3.4	2.6	15.6	5.1	16.4	8.8	12.1	5.1	1.7
CASPT2 (IPEA = 0.25)	47.9	48.2	5.4	4.4	0.0	0.3	0.8	2.8	3.9	1.1	3.2
MS-CASPT2 (IPEA = 0.25)	47.9	48.2	5.7	4.7	14.1	0.3	14.7	6.1	7.6	6.1	3.9
SF-CCSD	35.9	35.4	17.1	16.7	3.4	7.2	3.4	11.1	10.3	3.8	5.3
SF-CCSD(dT)	44.0	43.7	10.8	10.3	1.1	0.5	2.9	3.1	5.2	2.6	3.0

<sup>a</sup>All values are reported in kilocalories per mole. The  $\text{TS}_{\text{CIS}}$  and  $\text{TS}_{\text{TRANS}}$  barriers are computed as the energy difference between the transition state ( $\text{TS}_{\text{CIS}}$  or  $\text{TS}_{\text{TRANS}}$ ) and the corresponding  $\text{MIN}_{\text{CIS}}$  or  $\text{MIN}_{\text{TRANS}}$  intermediate. NPEs were computed along the composite (full) path which combines  $\text{MEP}_{\text{CIS}}$ , the CI seam, and  $\text{MEP}_{\text{TRANS}}$ , as well as just along the CI seam. The reference values (i.e. those belonging to MRCISD+Q) are highlighted in blue, while the values obtained at the level of theory with which the paths were generated are highlighted in orange.

adiabatic process occurring entirely on the  $S_1$  PES and exclusively at the CASPT2 level which, therefore, predicts the formation of two distinct  $S_1$  intermediates (i.e., corresponding to the  $\text{MIN}_{\text{CIS}}$  and  $\text{MIN}_{\text{TRANS}}$  structures). As for the CI seam (see center inset), we see a substantially different picture than that along the CASSCF CI seam. In fact, at the  $\text{CI}_{\text{BLA}}$  geometry, most methods (including MRCISD+Q) display a small or vanishing energy gap, indicating that this point is a CI for these methods (in fact, these methods displayed in Figures 5 and 6 generally appear to be more accurate than their other variants, and therefore reproduce the position of the MRCISD+Q CI well, as documented in our previous benchmark study<sup>8</sup>). However, this does not appear to be the case for  $\text{CI}_{\text{CIS}}$  and  $\text{CI}_{\text{TRANS}}$ , which, while being CI points at the CASPT2 (IPEA = 0.25) level of theory, do not remain so at the MRCISD+Q level. Therefore, to quantify such differences, we present in Table 2 again energy gaps at select structures and NPE values.

First, we discuss the energy gap at the  $\text{MIN}_{\text{CIS}}$  and  $\text{MIN}_{\text{TRANS}}$  structures. These structures are highly ( $\sim 70^\circ$ ) twisted around the C1–C2 single bond, resulting in a nitrogen-containing radical moiety and a conjugated radical cation moiety (see Scheme 2; such an electronic character is also supported by the geometry of these minima which display pyramidalization of the nitrogen and C1 carbon, as well as a small pyramidalization of the C2 carbon). The energy gaps at both  $\text{MIN}_{\text{CIS}}$  and  $\text{MIN}_{\text{TRANS}}$  are very similar to each other. The CASSCF gaps are not very different from MRCISD+Q, differing by 2.8–3.4 kcal/mol. Moreover, we find in this case that XMCQDPT2 is in very good agreement, but, oddly, this agreement decreases with the diagonal fit and  $F(\Gamma_{\text{ns}})$  variants (the origin of this disagreement is in the description of the  $S_0$  energy, and not  $S_1$ , which actually improves upon using the diagonal fit and  $F(\Gamma_{\text{ns}})$  variants as shown in Figure 6 and Figure S3 in the SI). QD-NEVPT2 is also in reasonable agreement with MRCISD+Q, as well as CASPT2 (especially when the IPEA shift is used, where the results become virtually identical to MRCISD+Q).

MS-CASPT2 results are identical to CASPT2. Finally, SF-CCSD significantly underestimates the energy gap, but the agreement with MRCISD+Q is improved upon introducing the triples correction, as expected.

In Table 2, we also present the energy barriers of  $\text{TS}_{\text{CIS}}$  and  $\text{TS}_{\text{TRANS}}$  with respect to  $\text{MIN}_{\text{CIS}}$  and  $\text{MIN}_{\text{TRANS}}$ , respectively. Such a calculation would be expected to be challenging for any method, since it would require a correct description of the intermediate electronic structure (diradicaloid with a positive charge on one side) as well as the transition state electronic character (where the electronic character is in between that of the  $S_1$  intermediate and the mixed diradical/charge transfer electronic character of the double-bond twisted  $S_1$  species). Indeed, we see a larger variation in the performance of different methods. All MRPT2 methods give a lower barrier than MRCISD+Q, with QD-NEVPT2 being the closest. Meanwhile, SF-CCSD significantly overestimates the barrier, while SF-CCSD(dT) still yields a high barrier but in closer agreement with MRCISD+Q.

In Table 2, we also present the energy gaps at  $\text{CI}_{\text{CIS}}$ ,  $\text{CI}_{\text{BLA}}$ , and  $\text{CI}_{\text{TRANS}}$ , as well as the NPE value along the CI seam for the CASPT2 paths.  $\text{CI}_{\text{BLA}}$  has degenerate  $S_0$  and  $S_1$  states at the MRCISD+Q, XMCQDPT2/diagonal fit, XMCQDPT2/ $F(\Gamma_{\text{ns}})$ , CASPT2 (IPEA = 0.25), MS-CASPT2 (IPEA = 0.25), and SF-CCSD(dT). These are the same methods that have an energy profile similar to MRCISD+Q along the BLA path in refs 8 and 11, and therefore have a similar geometry of the CI, as mentioned above. Meanwhile, XMCQDPT2 has an energy gap comparable with uncorrected MRCISD. QD-NEVPT2, as before, overestimates the energy gap, requiring a larger active space to properly describe this region,<sup>8</sup> while CASPT2 (IPEA = 0), MS-CASPT2 (IPEA = 0), and SF-CCSD appear more similar to CASSCF than MRCISD+Q. On the other hand, at the  $\text{CI}_{\text{CIS}}$  and  $\text{CI}_{\text{TRANS}}$  geometries, only CASPT2 (IPEA = 0.25) energies are degenerate. This may again be attributed to the absence of interaction between perturbed states in CASPT2,

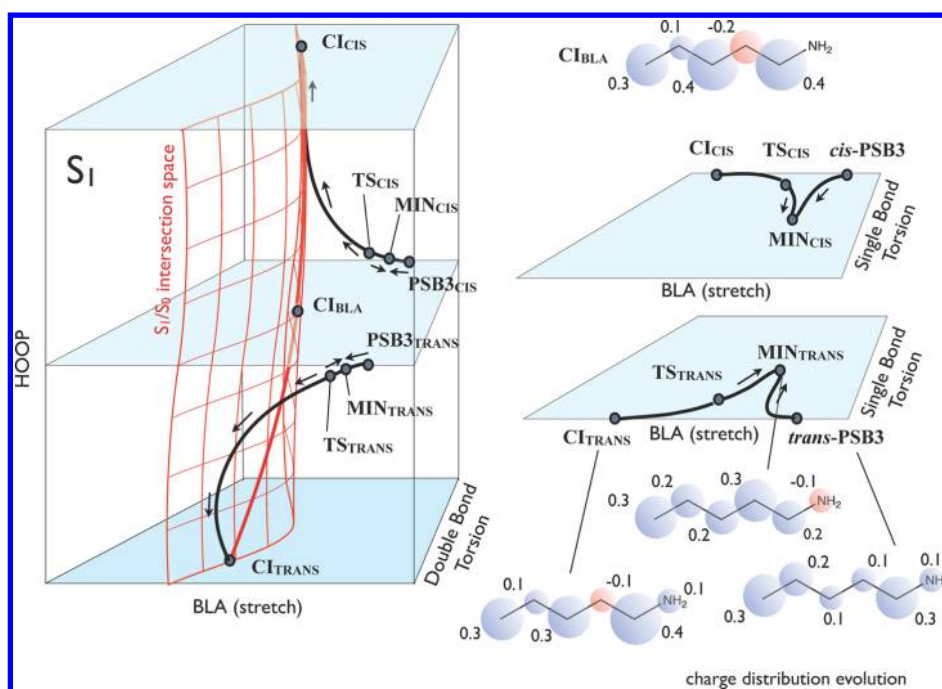


**Figure 7.** Schematic representation of the geometric deformations driven by the  $S_1$  force field of PSB3 as revealed by our composite CASPT2 paths. The located stationary points and conical intersections are indicated by circles. The arrows indicate the direction of the force along the paths which are described by bold black curves. (left) Structure of the three-dimensional configuration space defined by the BLA, HOOP, and  $C_2=C_3$  double bond torsion. Such space is proposed to contain a two-dimensional cross-section of the  $S_1/S_0$  intersection space spanning a combination of the torsional and HOOP modes. The cross-section must contain the mapped  $S_1/S_0$  intersection seam (see the bold red curve). The proportions are out of scale. (right) Structure of the two-dimensional configuration space defined by the BLA and  $C_1-C_2$  single bond torsion modes. The balloon diagrams at the top and bottom provide information on the evolution of the charge distribution for  $CI_{BLA}$  along the  $MEP_{TRANS}$  path (The charge evolution along  $MEP_{CIS}$  is similar to that along  $MEP_{TRANS}$  and is not shown). A numerical value is given for  $-CH-$ ,  $-CH_2-$ , and  $-NH_2$  groups with a total charge equal or larger than 0.1 in absolute value. Consistently with the charge transfer data in Figure 2B and 4B, the positive charge resides almost completely on the  $-C_2H=C_3H-C_4H=C_5H_2$  and  $=C_3H-C_4H=C_5H_2$  moieties in the  $MIN_{TRANS}/MIN_{CIS}$  and  $CI_{BLA}$  highly twisted structures respectively.

which results in large differences between CASPT2 and MS-CASPT2. So, while we find that CASPT2 degeneracy is maintained along the entire CI seam (see Figure 6), it is unique in this regard since other methods do not share the same CI seam shape, resulting in significantly larger CI seam NPE values in Table 2 than those found in Table 1.

Finally, a look at the NPE values along the composite CASPT2 path confirms the same main conclusions as those derived from the CASSCF path. Namely, we find that (1) CASSCF yields a large NPE value, but not as large as along the CASSCF path, (2) XMCQDPT2 performs relatively well, but the diagonal fit and  $F(\Gamma_{ns})$  variants perform better than the classical version in general, (3) QD-NEVPT2 has a larger NPE due to the CI seam region which, when ignored in computing the NPE, would reduce the NPE to 2.1 and 3.1 kcal/mol for  $S_0$  and  $S_1$ , respectively, (4) CASPT2 (IPEA = 0) and MS-CASPT2 (IPEA = 0) have a large NPE, partially due to artifacts in the CI seam region, but the NPE decreases when using the IPEA shift, and (5) SF-CCSD gives a large NPE, even larger than along the CASSCF path, but the NPE value is significantly reduced when the triples correction is included.

## CONCLUSIONS AND PERSPECTIVES

PSB3 has been a very popular reduced model system for rPSBs.<sup>1–4,8,14,15,20,57</sup> The photochemistry of rPSB has been and still is the focus of many experimental and computational studies not only due to its basic importance in photobiology (e.g., due to its role in the activation of visual, microbial

sensory, and ion-pumping pigments), but also due to the technology linked to its properties (e.g., for optogenetic actuators and probes<sup>58,59</sup> and for the possible development of molecular devices<sup>60</sup>). Thus, PSB3 has been used as a low-cost, minimal model of rPSB,<sup>1,2,4,61,62</sup> and also as a benchmark for understanding which approximate methods are best for describing the spectroscopy, photochemistry, or even thermal properties of visual pigments.<sup>8,11,12,14,15,20</sup>

In the current study, we expand the present knowledge on the excited state force field structure of PSB3 and benchmark the performance of MPRT2 and EOM-CC methods for such systems to understand the possible sources of inaccuracy when studying its photoisomerization. Accordingly, we have mapped the relevant  $S_1$  paths at both the CASSCF and CASPT2 levels of theory and documented the differences in the  $S_1$  PES of CASSCF and CASPT2. The geometric evolution driven by the computed  $S_1$  CASPT2 force field is pictorially summarized in Figure 7 where it is apparent that four different molecular modes (BLA, HOOP, double bond torsion, and single bond torsion) control the relaxation dynamics of the system. One remarkable difference is the existence of LE regions on the CASPT2  $S_1$  PES centered on single bond twisted structures, as already indicated by Valsson et al.<sup>20</sup> for PSB4 and by Send et al.<sup>22</sup> in different rPSB models. Such regions, which are not detected at the CASSCF level, need to be overcome or avoided in order for the double bond photoisomerization to occur. However, the results presented in this work have to be interpreted with caution. The differences between CASSCF and

CASPT2 in PSB3 are not necessarily present in rPSB in the gas-phase or in rPSB embedded in a protein environment. This is especially true when considering that the increased conjugation in the full chromophore would have an important effect on the size and stability of such an LE region, as well as the opsin environment and presence of counterions and polarizing residues. Furthermore, the pretwisting of the chromophore in the opsin environment might move the chromophore away from the LE region and prepare it for immediate isomerization around the double bond. In this sense, the CASSCF PES of PSB3, although incorrect, may turn out to be a more representative model of the rPSB PES because it is more consistent with its observed ultrafast isomerization mechanism, which would be expected to occur along a barrierless  $S_1$  path. In fact, while one study has successfully located an LE region and an  $S_1$  barrier in the PES of 11-*cis* locked rPSB, such a barrier was not located for natural rPSB.<sup>44</sup> The current model system indicates that such regions do, in principle, exist and further QM/MM studies on the full rPSB chromophore embedded in a protein environment can help us to better understand the significance of the environment on the relative stabilities of these regions with respect to the rest of the  $S_1$  PES. On the other hand, the potential interest of these regions for the control and engineering of rPSB photophysics appears to be high. Further stabilization of the LE region, perhaps via single bond twisting and/or via a suitable electrostatic potential imposed by the protein cavity, may lead to long-lived fluorescent states and, consequently, to the engineering of rhodopsin-based genetically encodable fluorescent probes, either from natural rhodopsins (e.g. see ref 44) or from a set of recently engineered artificial rhodopsin mimics,<sup>46–48</sup> (e.g. see ref 45).

The performance of MRPT2 and EOM-CC methods along the paths presented in this study confirm and extend the results of our previous benchmark studies.<sup>8,11</sup> We find that MRPT2 methods perform well when compared against MRCISD+Q. The performance of XMCQDPT2 is good but further improved by using the diagonal fit and  $F(\Gamma_{ns})$  variant, while QD-NEVPT2 performs very well along most regions of the PES with the exception of structures twisted along the double bond, where a larger active space is likely required to improve the quality of the zero-order CASSCF wave function. CASPT2 and MS-CASPT2 also perform well in most regions of the PES, with the exception of regions of strong mixing of the CASSCF wave function (near degeneracies) where artifacts may arise. The use of the IPEA parameter in CASPT2 and MS-CASPT2 improves their agreement with MRCISD+Q. Finally, while SF-CCSD provides a qualitatively accurate description of the PSB3 PES, the triples correction (dT) is needed for quantitatively accurate profiles which are in good agreement with MRCISD+Q.

As a more general conclusion, we believe that, together with the recently reported  $S_0$  PSB3 paths<sup>8</sup> which has also been investigated with different quantum chemical theories,<sup>8,11,12,63</sup> the  $S_1$  paths reported above provide a tractable system for the simultaneous benchmarking of ground and excited state organic reactivity. Such a benchmark system, including paths passing from closed to open-shell electronic structures and describing charge-transfer events and decays at conical intersection points, would expand the testing of advanced electronic structure methods from vertical excitation energies (see for instance ref 64) to entire PES regions.

## ■ ASSOCIATED CONTENT

### ■ Supporting Information

Supporting figures showing the energy profiles of all methods along the composite CASSCF and CASPT2 paths. Tables with CASSCF and MRCISD+Q energies along the CASSCF path and CASPT2 and MRCISD+Q energies along the CASPT2 path. Cartesian coordinates of points along the two composite paths. This material is available free of charge via the Internet at <http://pubs.acs.org/>.

## ■ AUTHOR INFORMATION

### Corresponding Author

\*E-mail: [molivuc@bgnet.bgsu.edu](mailto:molivuc@bgnet.bgsu.edu).

### Notes

The authors declare no competing financial interest.

## ■ ACKNOWLEDGMENTS

We thank Prof. Nicolas Ferré for a critical reading of the manuscript. This work was supported by the Bowling Green State University. M.O. is grateful to the Center for Photochemical Sciences of Bowling Green State University for start-up funds, the Human Frontier Science Program Organization under grant RGP0049/385 2012, National Science Foundation for grant CHE-1152070. The COST-CMTS Action CM1002 “Convergent Distributed Environment for Computational Spectroscopy (CODECS)” is also acknowledged. R.L. thanks the Swedish Research Council (VR) for financial support. A.I.K. acknowledges support of the Department of Energy (DE-FG02-05ER15685). A.G. is grateful for financial support by Russian Ministry of Education and Science through Contract No. 07.514.11.4128 and by RFBR through Grant No. 11-03-01214. C.A. has been financed by the Italian MIUR through its PRIN 2009 funds. We are grateful to the Ohio Supercomputer Center, NSF-TeraGrid (now XSEDE), and CINECA for granted computer time.

## ■ REFERENCES

- (1) Garavelli, M.; Celani, P.; Bernardi, F.; Robb, M. A.; Olivucci, M. J. *Am. Chem. Soc.* **1997**, *119*, 6891–901.
- (2) Garavelli, M.; Bernardi, F.; Robb, M. A.; Olivucci, M. J. *Mol. Struct. (Theochem)*. **1999**, *463*, 59–64.
- (3) Sinicropi, A.; Migani, A.; De Vico, L.; Olivucci, M. *Photochem. Photobiol. Sci.* **2003**, *2*, 1250–5.
- (4) Barbatti, M.; Ruckebauer, M.; Szymczak, J. J.; Aquino, A. J.; Lischka, H. *Phys. Chem. Chem. Phys.* **2008**, *10*, 482–94.
- (5) Butscher, W.; Shih, S. K.; Buenker, R. J.; Peyerimhoff, S. D. *Chem. Phys. Lett.* **1977**, *52*, 457–62.
- (6) Knowles, P. J.; Werner, H. J. *Theo. Chem. Acc.* **1992**, *84*, 95–103.
- (7) Langhoff, S. R.; Davidson, E. R. *Int. J. Quantum Chem.* **1974**, *8*, 61–72.
- (8) Gozem, S.; Huntress, M.; Schapiro, I.; Lindh, R.; Granovsky, A. A.; Angeli, C.; Olivucci, M. J. *Chem. Theo. Comp.* **2012**, *8*, 4069–4080.
- (9) Stanton, J. F.; Gauss, J. In *Advances in Chemistry and Physics*; Prigogine, I., Rice, S. A., Eds.; John Wiley & Sons Inc.: Hoboken, NJ, **2003**; Vol. 125, pp 101–146.
- (10) Krylov, A. I. *Annu. Rev. Phys. Chem.* **2008**, *59*, 433–62.
- (11) Gozem, S.; Krylov, A. I.; Olivucci, M. J. *Chem. Theo. Comp.* **2013**, *9*, 284–92.
- (12) Xu, X.; Gozem, S.; Olivucci, M.; Truhlar, D. G. *J. Phys. Chem. Lett.* **2013**, *4*, 253–8.
- (13) Migani, A.; Robb, M. A.; Olivucci, M. J. *Am. Chem. Soc.* **2003**, *125*, 2804–8.
- (14) Page, C. S.; Olivucci, M. J. *Comput. Chem.* **2003**, *24*, 298–309.
- (15) Fantacci, S.; Migani, A.; Olivucci, M. J. *Phys. Chem. A* **2004**, *108*, 1208–13.



- (16) Wanko, M.; Garavelli, M.; Bernardi, F.; Niehaus, T. A.; Frauenheim, T.; Elstner, M. *J. Chem. Phys.* **2004**, *120*, 1674–92.
- (17) Schautz, F.; Buda, F.; Filippi, C. *J. Chem. Phys.* **2004**, *121*, 5836–44.
- (18) Keal, T. W.; Wanko, M.; Thiel, W. *Theo. Chem. Acc.* **2009**, *123*, 145–56.
- (19) Send, R.; Sundholm, D. *J. Phys. Chem. A* **2007**, *111*, 8766–73.
- (20) Valsson, O.; Filippi, C. *J. Chem. Theo. Comp.* **2010**, *6*, 1275–92.
- (21) Conte, A. M.; Guidoni, L.; Del Sole, R.; Pulci, O. *Chem. Phys. Lett.* **2011**, *515*, 290–5.
- (22) Send, R.; Sundholm, D.; Johansson, M. P.; Pawlowski, F. *J. Chem. Theo. Comp.* **2009**, *5*, 2401–14.
- (23) Ghigo, G.; Roos, B. O.; Malmqvist, P. K. *Chem. Phys. Lett.* **2004**, *396*, 142–9.
- (24) Levine, B. G.; Ko, C.; Quenneville, J.; Martínez, T. J. *Mol. Phys.* **2006**, *104*, 1039–1051.
- (25) Werner, H. J.; Knowles, P. J.; Knizia, G.; Manby, F. R.; Schütz, M.; Celani, P.; Korona, T.; Lindh, R.; Mitrushenkov, A.; Rauhut, G.; Shamassundar, K. R.; Adler, T. B.; Amos, R. D.; Bernhardsson, A.; Berning, A.; Cooper, D. L.; Deegan, M. J. O.; Dobbyn, A. J.; Eckert, F.; Goll, E.; Hampel, C.; Hesselmann, A.; Hetzer, G.; Hrenar, T.; Jansen, G.; Köppl, C.; Liu, Y.; Lloyd, A. W.; Mata, R. A.; May, A. J.; McNicholas, S. J.; Meyer, W.; Mura, M. E.; Nicklass, A.; O'Neill, D. P.; Palmieri, P.; Pflüger, K.; Pitzer, R.; Reiher, M.; Shiozaki, T.; Stoll, H.; Stone, A. J.; Tarroni, R.; Thorsteinsson, T.; Wang, M.; Wolf, A. *MOLPRO*, version 2010.1, a package of ab initio programs; Cardiff University: Cardiff, U.K.; Universität Stuttgart: Stuttgart, Germany, 2010.
- (26) Werner, H. J.; Knowles, P. J. *J. Chem. Phys.* **1988**, *89*, 5803.
- (27) Werner, H. J.; Kállay, M.; Gauss, J. *J. Chem. Phys.* **2008**, *128*, 034305.
- (28) Andersson, K.; Malmqvist, P.; Roos, B. O. *J. Chem. Phys.* **1992**, *96*, 1218.
- (29) Granovsky, A. A. *J. Chem. Phys.* **2011**, *134*, 214113.
- (30) Angeli, C.; Cimiraglia, R.; Evangelisti, S.; Leininger, T.; Malrieu, J. P. *J. Chem. Phys.* **2001**, *114*, 10252.
- (31) Angeli, C.; Pastore, M.; Cimiraglia, R. *Theor. Chem. Acc.* **2007**, *117*, 743–54.
- (32) Finley, J.; Malmqvist, P.; Roos, B. O.; Serrano-Andrés, L. *Chem. Phys. Lett.* **1998**, *288*, 299–306.
- (33) Aquilante, F.; De Vico, L.; Ferré, N.; Ghigo, G.; Malmqvist, P. A.; Neogrády, P.; Pedersen, T. B.; Pitonák, M.; Reiher, M.; Roos, B. O.; Serrano-Andrés, L.; Urban, M.; Veryazov, V.; Lindh, R. *J. Comput. Chem.* **2010**, *31*, 224–47.
- (34) Angeli, C.; Borini, S.; Cestari, M.; Cimiraglia, R. *J. Chem. Phys.* **2004**, *121*, 4043–9.
- (35) Granovsky, A. A. *Firefly*, version 8.0.0, 2013; <http://classic.chem.msu.su/gran/firefly/index.html>.
- (36) Krylov, A. I. *Chem. Phys. Lett.* **2001**, *338*, 375–84.
- (37) Slipchenko, L. V.; Krylov, A. I. *J. Chem. Phys.* **2002**, *117*, 4694.
- (38) Levchenko, S. V.; Krylov, A. I. *J. Chem. Phys.* **2004**, *120*, 175–85.
- (39) Krylov, A. I. *Acc. Chem. Res.* **2006**, *39*, 83–91.
- (40) Manohar, P. U.; Krylov, A. I. *J. Chem. Phys.* **2008**, *129*, 194105.
- (41) Shao, Y.; Molnar, L. F.; Jung, Y.; Kussmann, J.; Ochsenfeld, C.; Brown, S. T.; Gilbert, A. T.; Slipchenko, L. V.; Levchenko, S. V.; O'Neill, D. P.; DiStasio, R. A.; Lochan, R. C.; Wang, T.; Beran, G. J.; Besley, N. A.; Herbert, J. M.; Lin, C. Y.; Van Voorhis, T.; Chien, S. H.; Sodt, A.; Steele, R. P.; Rassolov, V. A.; Maslen, P. E.; Korambath, P. P.; Adamson, R. D.; Austin, B.; Baker, J.; Byrd, E. F.; Dachsel, H.; Doerksen, R. J.; Dreuw, A.; Dunietz, B. D.; Dutoi, A. D.; Furlani, T. R.; Gwaltney, S. R.; Heyden, A.; Hirata, S.; Hsu, C. P.; Kedziora, G.; Khalliulin, R. Z.; Klunzinger, P.; Lee, A. M.; Lee, M. S.; Liang, W.; Lotan, I.; Nair, N.; Peters, B.; Proynov, E. I.; Pieniazek, P. A.; Rhee, Y. M.; Ritchie, J.; Rosta, E.; Sherrill, C. D.; Simmonett, A. C.; Subotnik, J. E.; Woodcock, H. L.; Zhang, W.; Bell, A. T.; Chakraborty, A. K.; Chipman, D. M.; Keil, F. J.; Warshel, A.; Hehre, W. J.; Schaefer, H. F.; Kong, J.; Krylov, A. I.; Gill, P. M.; Head-Gordon, M. *Phys. Chem. Chem. Phys.* **2006**, *8*, 3172–91.
- (42) González-Luque, R.; Garavelli, M.; Bernardi, F.; Merchán, M.; Robb, M. A.; Olivucci, M. *Proc. Natl. Acad. Sci. U.S.A.* **2000**, *97*, 9379–84.
- (43) Andruniów, T.; Ferré, N.; Olivucci, M. *Proc. Natl. Acad. Sci. U.S.A.* **2004**, *101*, 17908–13.
- (44) Frutos, L. M.; Andruniów, T.; Santoro, F.; Ferré, N.; Olivucci, M. *Proc. Natl. Acad. Sci. U.S.A.* **2007**, *104*, 7764–9.
- (45) Laricheva, E. N.; Gozem, S.; Rinaldi, S.; Melaccio, F.; Valentini, A.; Olivucci, M. *J. Chem. Theo. Comp.* **2012**, *8*, 2559–63.
- (46) Huntress, M.; Gozem, S.; Malley, K. R.; Jailaubekov, A. E.; Vasileiou, C.; Vengris, M.; Geiger, J. H.; Borhan, B.; Schapiro, I.; Larsen, D. S.; Olivucci, M. *J. Phys. Chem. B* **2013**, *117*, 10053–10070.
- (47) Crist, R. M.; Vasileiou, C.; Rabago-Smith, M.; Geiger, J. H.; Borhan, B. *J. Am. Chem. Soc.* **2006**, *128*, 4522–4523.
- (48) Vasileiou, C.; Vaezeslami, S.; Crist, R. M.; Rabago-Smith, M.; Geiger, J. H.; Borhan, B. *J. Am. Chem. Soc.* **2007**, *129*, 6140–6148.
- (49) Wang, W.; Nossoni, Z.; Berbasova, T.; Watson, C. T.; Yapici, I.; Lee, K. S.; Vasileiou, C.; Geiger, J. H.; Borhan, B. *Science* **2012**, *338*, 1340–1343.
- (50) Bonačić-Koutecký, V.; Koutecký, J.; Michl, J. *Angew. Chem., Int. Ed.* **1987**, *26*, 170–89.
- (51) Rotkiewicz, K.; Grellmann, K. H.; Grabowski, Z. R. *Chem. Phys. Lett.* **1973**, *19*, 315–8.
- (52) Grabowski, Z. R.; Rotkiewicz, K.; Rettig, W. *Chem. Rev.* **2003**, *103*, 3899–4032.
- (53) Schapiro, I.; Ryazantsev, M. N.; Frutos, L. M.; Ferré, N.; Lindh, R.; Olivucci, M. *J. Am. Chem. Soc.* **2011**, *133*, 3354–64.
- (54) Salem, L. *Acc. Chem. Res.* **1979**, *12*, 87–92.
- (55) Weingart, O.; Altoè, P.; Stenta, M.; Bottoni, A.; Orlandi, G.; Garavelli, M. *Phys. Chem. Chem. Phys.* **2011**, *13*, 3645–8.
- (56) Angeli, C.; Pastore, M. *J. Chem. Phys.* **2011**, *134*, 184302.
- (57) Mori, T.; Nakano, K.; Kato, S. *J. Chem. Phys.* **2010**, *133*, 064107.
- (58) Toettcher, J. E.; Voigt, C. A.; Weiner, O. D.; Lim, W. A. *Nat. Methods* **2011**, *8*, 35–8.
- (59) Pastrana, E. *Nat. Methods* **2011**, *8*, 447.
- (60) Sinicropi, A.; Martin, E.; Ryazantsev, M.; Helbing, J.; Briand, J.; Sharma, D.; Léonard, J.; Haacke, S.; Cannizzo, A.; Chergui, M.; Zanirato, V.; Fusi, S.; Santoro, F.; Basosi, R.; Ferré, N.; Olivucci, M. *Proc. Natl. Acad. Sci. U.S.A.* **2008**, *105*, 17642–7.
- (61) Weingart, O. *Chem. Phys.* **2008**, *349*, 348–55.
- (62) Ruckebauer, M.; Barbatti, M.; Müller, T.; Lischka, H. *J. Phys. Chem. A* **2013**, *117*, 2790–9.
- (63) Huix-Rotllant, M.; Filatov, M.; Gozem, S.; Schapiro, I.; Olivucci, M.; Ferre, N. *J. Chem. Theo. Comp.* **2013**, *9*, 3917–3932.
- (64) Schapiro, I.; Sivalingam, K.; Neese, F. *J. Chem. Theo. Comp.* **2013**, *9*, 3567–3580.